Magnetic Switching in Weyl Semimetal-Superconductor Heterostructures*

Narayan Mohanta,[1,†] A. Taraphder,[2] Elbio Dagotto,[1,3] and Satoshi Okamoto[1]

[1] *Material Science and Technology Division, Oak Ridge National Laboratory, Oak Ridge, TN 37831, USA*
[2] *Department of Physics and Center for Theoretical Studies, Indian Institute of Technology Kharagpur, W.B. 721302, India*
[3] *Department of Physics and Astronomy, The University of Tennessee, Knoxville, TN 37996, USA*

We present a new switching mechanism that utilizes the proximity coupling between the surface spin texture of a Weyl semimetal and a superconductor, in a Weyl semimetal/superconductor/Weyl semimetal trilayer heterostructure. We show that the superconductivity in the middle layer can be fully suppressed by the surface spin texture of the Weyl semimetals in the presence of an external magnetic field, but it can be recovered again by only changing the field direction. The restoration of the middle-layer superconductivity indicates a sharp transition to a low-resistance state. This sharp switching effect, realizable using a Weyl semimetal because of its strong spin-momentum locking and surface spin polarization, is a promising avenue for novel superconducting spin-valve applications.

Introduction.—A three-dimensional Weyl semimetal (WSM) is strikingly different from other classes of materials with non-trivial band topology because of the presence of surface Fermi arcs [1, 2] which prompted the observation of a plethora of intriguing properties, such as quantum oscillations in magnetoresistance [3–5] and chiral magnetic effect [6–23]. The Fermi arcs exhibit a spin texture with a strong spin-momentum locking which leads to a spin polarization (up to 80% for TaAs) on the surface of the WSMs [24–26]. By introducing a superconducting gap in the WSM, the superconductor (SC) inherits the non-trivial topology of the electronic structure of the WSM, giving rise to unconventional properties such as finite-momentum pairing and Majorana zero modes [27–39]. At a WSM/SC interface, superconductivity is proposed to be induced by the proximity effect inside the WSM near the interface [40]. Despite a few studies on the proximity effect of the superconductivity inside the WSM in a WSM/SC interface, the *inverse* proximity effect of the WSM surface magnetization on the superconductivity remains unexplored.

In this work, we demonstrate a new switching effect induced by the interplay between superconductivity and magnetization at a WSM/SC interface, in the presence of an external magnetic field. We consider a trilayer heterostructure, with an *s*-wave SC sandwiched between two WSM slabs in such a way that the top and the bottom WSMs have opposite alignments of the Fermi arcs. In this geometry, the WSM surfaces, on both sides of the SC, have a net spin polarization *in the same direction*. The superconductivity in the middle SC layer is suppressed completely by the joint pair-breaking effect of the WSM surface magnetization and the magnetic field. However, by rotating the field, the net magnetization of the WSM surfaces drops to a smaller value and the fully-suppressed superconductivity restores again, indicating a sharp transition to the zero-resistance state in the middle SC layer. Such a magnetic switching has the potential to advance the spin-valve applications that at present employ trilayer heterostructors of ferromagnets (FMs) and SCs [41–57].

In the state-of-the-art spin-valve switching devices,

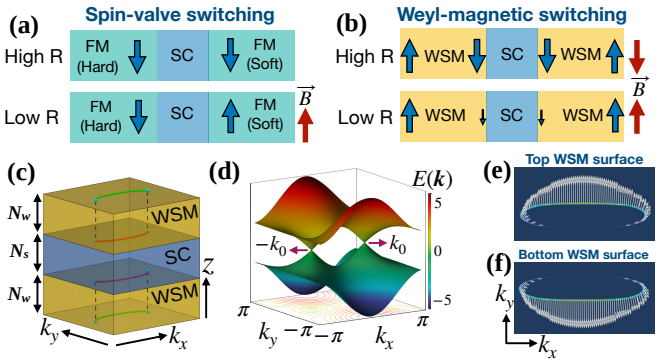

FIG. 1. (a) Standard spin-valve switching mechanism involving a FM/SC/FM trilayer. The blue arrows denote the magnetization in the FMs. (b) Proposed switching mechanism using a WSM/SC/WSM trilayer. The blue arrows denote the net surface magnetization. (c) Schematic of the considered trilayer heterostructure. The red and the green lines at the surfaces of the WSMs denote the conjugate Fermi arcs. (d) Bulk bands of a WSM with broken time-reversal symmetry, showing the pair of the Weyl nodes at $(\pm k_0,0,0)$. $E(\mathbf{k})$ are the eigenvalues of Hamiltonian (1) at k_z=0 (in units of t, a parameter mentioned in the text). (e)-(f) The computed Fermi arcs (the momentum-resolved density of states at energy $E(\mathbf{k})$=−0.3t) and spin textures (white arrows) on the opposite surfaces of an isolated WSM slab of thickness N_w=15.

† E-mail: mohantan@ornl.gov

involving a FM(hard)/SC/FM(soft) trilayer, as shown in Fig. 1(a), the resistance R_p, in the parallel polarization of the top and bottom FMs near the superconducting transition temperature T_c, is larger than the resistance R_{ap} in the anti-parallel case. The magnetic field flips the polarization in the soft FM and produces a transition to a low-resistance state. In our proposed WSM-based geometry, shown in Figs. 1(b) and (c), the net magnetization of the WSM surfaces on both sides of the SC drops to a smaller value when the magnetic field is applied opposite to the spin polarization direction. The field rotation drives the middle SC to the zero-resistance state, implying a low resistance in the WSM/SC/WSM trilayer.

Model and method.—We consider a type-I WSM with broken time-reversal symmetry and having only two Weyl points, described by the following Hamiltonian [58]

$$\mathcal{H}_w = \sum_{\mathbf{k}} - \Big[\{ m(2 - \cos k_y - \cos k_z) + 2t_x(\cos k_x - \cos k_0) \} \sigma_x - (2t \sin k_y)\sigma_y - (2t \sin k_z)\sigma_z - \mu_w \mathcal{I} \Big], \quad (1)$$

where m, t_x, and t are parameters that describe the bulk band dispersion, μ_w is the chemical potential of the WSM, $\boldsymbol{\sigma} \equiv (\sigma_x, \sigma_y, \sigma_z)$ represents the Pauli matrices, $\mathcal{I}$ is the 2×2 identity matrix, and $\mathbf{k} \equiv (k_x, k_y, k_z)$ denotes the momentum in three dimensions. The Weyl nodes are located at $(\pm k_0, 0, 0)$ as depicted in Fig. 1(d). In Fig. 1(e) and (f), we show the Fermi arcs and the spin texture on the opposite surfaces of an isolated WSM slab [59]. The parameters t=1, m=2t, k_0=π/2, t_x=t, used in Ref. [58], are kept fixed throughout this paper, with no qualitative change in our conclusions for other choices.

To describe the proximity-induced superconductivity in the WSM, we express $\mathcal{H}_w$ in the Nambu-spinor basis $\Psi_{\mathbf{k}} = \left(c_{\mathbf{k},\uparrow}, c_{\mathbf{k},\downarrow}, c^\dagger_{-\mathbf{k},\uparrow}, c^\dagger_{-\mathbf{k},\downarrow}\right)^T$ as

$$\mathcal{H}^{sc}_w = \sum_{\mathbf{k}} \begin{pmatrix} \mathcal{H}_w & i\sigma_y \Delta_w \\ -i\sigma_y \Delta^*_w & -\mathcal{H}^*_w \end{pmatrix}, \quad (2)$$

where $\Delta_w = \langle c_{\mathbf{k},\uparrow} c_{-\mathbf{k},\downarrow} \rangle$ is the proximity-induced s-wave pairing amplitude in the WSM. Although a small finite-momentum pairing and a triplet pairing could also be induced in the WSM, we focus only on singlet pairing at zero center-of-mass momentum which is the dominant pairing channel and relevant to the present study.

We consider BCS-type electron pairing in the middle SC slab, expressed by the following Hamiltonian [59]

$$\mathcal{H}_s = - \sum_{\mathbf{k},\sigma} \Big[2t_s(\cos k_x + \cos k_y + \cos k_z) + \mu_s \Big] d^\dagger_{\mathbf{k},\sigma} d_{\mathbf{k},\sigma} + \sum_{\mathbf{k}} (\Delta_s d^\dagger_{\mathbf{k},\uparrow} d^\dagger_{-\mathbf{k},\downarrow} + H.c.) + \frac{N\Delta_s^2}{|U_0|}, \quad (3)$$

where t_s is the hopping amplitude, μ_s the chemical potential, $\Delta_s = U_0 \langle d_{\mathbf{k},\uparrow} d_{-\mathbf{k},\downarrow} \rangle$ the s-wave pairing amplitude in the SC, U_0 the pairwise attractive interaction strength, and N is the total number of momenta in the Brillouin zone. We set t_s=t and U_0=$-t$ everywhere, without losing generality.

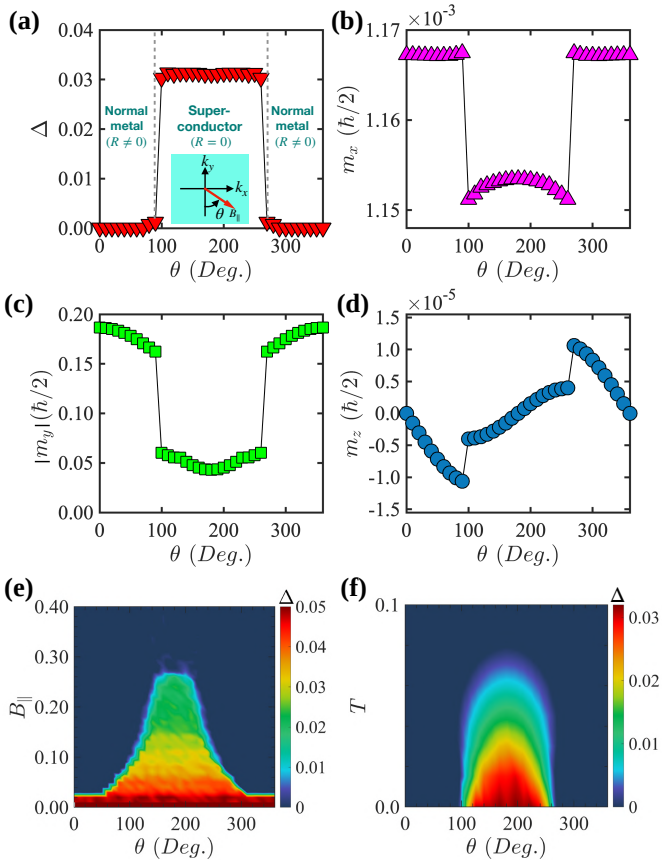

FIG. 2. (a) Superconducting pairing amplitude Δ (in units of t), averaged over all layers of the WSM/SC/WSM heterostructure, plotted as a function of the magnetic-field angle θ which is measured with respect to the $-k_y$ direction, as shown in the inset. (b)-(d) θ-variation of the magnetization components m_x, m_y, m_z at the bottom surface of the top WSM slab. The magnetic field and the temperature in plots (a)-(d) are $B_\parallel$=0.1t and T=0, respectively. (e), (f) Variation of Δ (number in the colorbar) with the angle θ and the magnetic-field amplitude $B_\parallel$ (at T=0) in (e), and temperature T (at $B_\parallel$=0.1t) in (f). Parameters used are N_w=15, N_s=15, t_{tun}=t, μ_w=$-0.3t$ and μ_s=0.1t.

The Hamiltonian for the heterostructure is constructed by transforming the Hamiltonians $\mathcal{H}^{sc}_w$ and $\mathcal{H}_s$ into the slab geometry [59], with N_s layers in the SC slab and N_w layers in both (top and bottom) WSM slabs. Open boundary conditions are imposed along the stacking direction (the z axis), so that k_x and k_y are good quantum numbers for the description in each layer. The coupling between the WSM and the SC slabs at the WSM/SC interfaces is described by the following tunneling Hamiltonian

$$\mathcal{H}_{tun} = - \sum_{\mathbf{k}^\parallel, l_z, \sigma} (t_{tun} c^\dagger_{\mathbf{k}^\parallel,\sigma,l_z} d_{\mathbf{k}^\parallel,\sigma,l_z+1} + H.c.), \quad (4)$$

where l_z is the vertical layer index at the interface, t_{tun} is the tunneling amplitude between the WSMs and the SC and $\mathbf{k}^\parallel \equiv (k_x, k_y)$ is the momentum in the k_x-k_y plane.

The external magnetic field, applied uniformly in all the layers of the heterostructure, is included as a Zeeman

exchange coupling term

$$\mathcal{H}_z = \sum_{\mathbf{k}^{\parallel},l_z,\sigma,\sigma'} (\mathbf{B}\cdot\boldsymbol{\sigma}_{\sigma\sigma'}) c^{\dagger}_{\mathbf{k}^{\parallel},\sigma,l_z} c_{\mathbf{k}^{\parallel},\sigma',l_z}, \qquad (5)$$

where $\mathbf{B}=(B_{\parallel}\cos\theta, B_{\parallel}\sin\theta, 0)$, $B_{\parallel}$ is the strength of the magnetic field (in energy unit), and θ is the field angle. Henceforth, all energy terms are expressed in units of the parameter t defined in Eq. (1).

The superconducting order parameter, i.e. the pairing amplitude Δ_{l_z} at each layer l_z, is calculated self-consistently by minimizing the free energy of the heterostructure [59]. The average pairing amplitude for the heterostructure is then obtained via $\Delta=(1/(N_s+2N_w))\sum_{l_z}\Delta_{l_z}$. In each layer l_z, the spin texture $(m_{\mathbf{k}^{\parallel},x}, m_{\mathbf{k}^{\parallel},y}, m_{\mathbf{k}^{\parallel},z})$ is obtained by computing the spin-expectation values at each momentum $\mathbf{k}^{\parallel}$ and the average magnetization components (m_x, m_y, m_z) are obtained by taking average in the two-dimensional Brillouin zone [59].

Origin of the magnetic switching.—The main concept introduced here, the magnetic switching at the WSM/SC interfaces, involves the strong interplay between superconductivity and the WSM surface magnetization; the latter competes against the electron pairing near the interfaces. The magnetic field $B_{\parallel}$=0.1t ($<B^c_{\parallel}\approx$0.3t, the critical field for the SC), applied along θ=0°, cooperates with the WSM surface magnetization to *completely* suppress superconductivity. Remarkably, by changing the field direction, the average pairing amplitude Δ re-emerges and jumps from nearly zero to a finite value at $\theta\approx$100°. The order parameter Δ remains almost constant within a range 100°$\lesssim\theta\lesssim$260°, as shown in Fig. 2(a). This sudden restoration of the superconductivity, only by changing the field angle, implies a switching from a finite-resistance to a low-resistance state. *This magnetic field-driven 'switching' is the main finding of this paper.*

To understand the origin of this switching effect, we explore the θ-dependence of the magnetization components. Interestingly, we find similar discontinuous jumps in the magnetization components at the WSM terminating layers, adjacent to the SC slab, as shown in Figs. 2(b)-(d). The in-plane magnetization components m_x and m_y drop to relatively smaller values within the same range 100°$\lesssim\theta\lesssim$260°. The out-of-plane component m_z also undergoes sharp transitions at the critical field angles $\theta_{c1}\approx$100° and $\theta_{c2}\approx$260°, as shown in Fig. 2(d). This finding underlines the strong interplay between the magnetism in the WSM surface and the superconductivity near the WSM/SC interfaces. The θ-variation of Δ with the field amplitude $B_{\parallel}$, in Fig. 2(e), suggests that there is a lower and an upper critical field and the switching occurs in between. The lower critical field is the required field to fully suppress the superconductivity at certain ranges of θ values, while the upper critical field is the largest field above which the reappearance of superconductivity is unanticipated. Temperature variation of Δ, in Fig. 2(f), suggests that the switching effect appears predominantly at low temperatures, below the superconducting T_c of the middle SC.

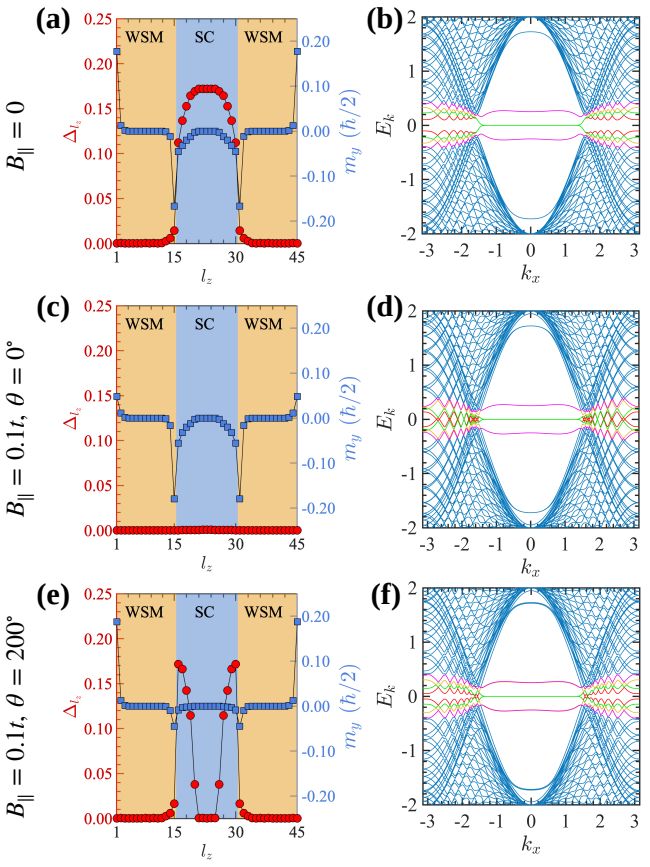

FIG. 3. (a),(c),(e) Variation of the superconducting pairing amplitude Δ_{l_z} (left vertical axis) and y component of magnetization m_y (right vertical axis) with the layer index l_z at (a) magnetic field $B_{\parallel}$=0, (c) $B_{\parallel}$=0.1t, θ=0°, and (e) $B_{\parallel}$=0.1t, θ=200°. (b), (d), and (f) show the corresponding energy spectrum of the WSM/SC/WSM heterostructure at k_y=0. The energy levels in red, green, yellow and magenta originate primarily from the surfaces of the WSMs. Parameters are the same as in Fig. 2.

To explore the interplay between the WSM surface magnetization and the superconductivity, we plot the layer-resolved pairing amplitude Δ_{l_z}, and the dominant magnetization component m_y, in Figs. 3(a), (c) and (e), at different field scenarios and the corresponding spectrum in Figs. 3(b), (d) and (f). At $B_{\parallel}$=0, a small pairing amplitude is induced inside the WSMs, by proximity effect, but this induced superconductivity is limited to the near vicinity of the interfaces [40]. Conversely, the pairing amplitude inside the SC is also suppressed near the interfaces since the WSM surface magnetism penetrates inside the SC and affects the superconductivity. At a finite magnetic field $B_{\parallel}$=0.1t, applied along θ=0°, the superconductivity is completely suppressed, as shown in Fig. 3(c), by the combined pair-breaking effect of the magnetic field and the WSM surface magnetization. However, when the field is applied along θ=200°, i.e. opposite to the WSM surface magnetization, the net magnetization of the WSM

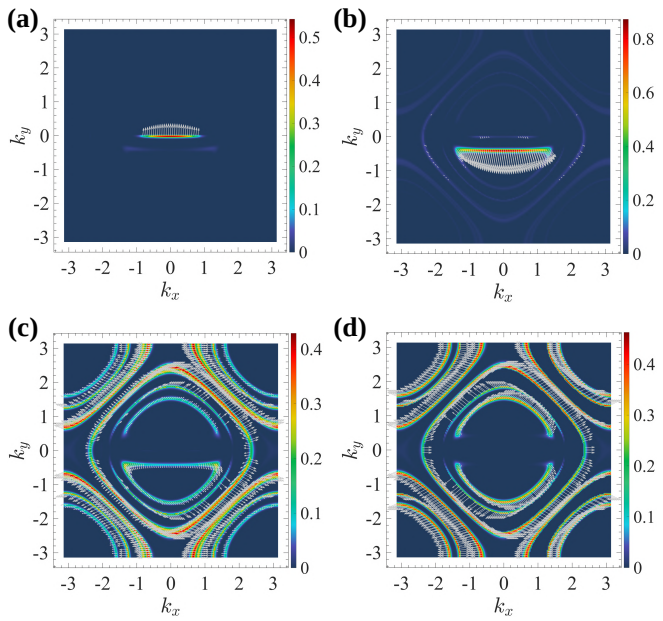

FIG. 4. Momentum-resolved density of states $A(\mathbf{k}^{\parallel},E)$ (colorbar) and spin texture (arrows show the in-plane spin-expectation values $m_{\mathbf{k}^{\parallel},x}$ and $m_{\mathbf{k}^{\parallel},y}$) at energy E=−0.3t at zero magnetic field and different layers of the WSM/SC/WSM heterostructure. (a) l_z=1 (top layer of the top WSM), (b) l_z=15 (bottom layer of the top WSM), (c) l_z=16 (top layer of the SC), (d) l_z=18 (inside the SC but close to the top WSM/SC interface). Parameters are the same as in Fig. 2.

surface drops drastically which enables the reappearance of the superconductivity in the near vicinity of the WSM/SC interfaces, as depicted in Fig. 3(e). Similar reappearance of the superconductivity takes place within the angle range $100°\lesssim\theta\lesssim260°$. The profile of Δ_{l_z} remains nearly unchanged within this range of θ [59]. The sharp transitions, at the critical angles, is possible in a WSM because of its strong spin-momentum locking which makes the spin texture of the Fermi arcs quite robust against the external magnetic field, applied at an angle outside this angle range. Within this range, the magnetic field overcomes the spin-momentum locking and significantly reduces the in-plane magnetization components [59].

The energy spectrum of the heterostructure at $B_{\parallel}$=0, in Fig. 3(b), shows that two pairs of energy levels (green and red) exhibit flat zero-energy states within the Fermi-arc region ($|k_x|\lesssim k_0$) while two other pairs (magenta and yellow) are gapped out at finite energies. These low-energy bands originate from the hybridization between the surface states in the WSMs and the SC slabs. The spectrum changes when a magnetic field $B_{\parallel}$=0.1t is applied along θ=0°, as shown in Fig. 3(d). Particularly, outside the flat-band region ($|k_x|>k_0$), the red and the green bands do not have an energy gap at θ=0° (Fig. 3(d)) and a finite energy gap at θ=200° (Fig. 3(f)). These two angles belong to the two different states *viz.* the suppressed and recovered superconducting states, shown before in Fig. 2(a). Evidently, the electronic spectra also reveals a signature of these different states.

To gain insight on the critical field angles θ_{c1} and θ_{c2}, we calculated the spin texture and the momentum-resolved density of states $A(\mathbf{k}^{\parallel},E)=\sum_{\sigma,\lambda}|c_{\mathbf{k}^{\parallel},\sigma,l_z}|^2\delta(E-E_{\mathbf{k}^{\parallel}\lambda})+|c^{\dagger}_{-\mathbf{k}^{\parallel},\sigma,l_z}|^2\delta(E+E_{-\mathbf{k}^{\parallel}\lambda})$ at different layers of the heterostructure ($c_{\mathbf{k}^{\parallel},\sigma,l_z}$ is replaced by $d_{\mathbf{k}^{\parallel},\sigma,l_z}$ for the SC layers). In Fig. 4, we show the spin texture at four different layers at $B_{\parallel}$=0. The top surface of the top WSM (l_z=1) reveals a Fermi arc and spin texture [Fig. 4(a)] at energy E=−0.3t(=μ_w), similar to the case of an isolated WSM slab, shown earlier in Fig. 1(e). On the other hand, Fig. 4(d), shows the constant-energy contours and spin texture at a SC layer (l_z=18), slightly below the top WSM/SC interface, at energy E=−0.3t ($<\mu_s$) showing the electron-like and hole-like contours. Notably, two electron-like contours around $\mathbf{k}^{\parallel}$=**0** are disconnected along the k_y=0 direction, influenced by the Fermi arc in the neighboring WSM layer (l_z=15). The proximity effect of the Fermi arc is prominent at the top SC layer (l_z=16) [in Fig. 4(c)] which also develops a Fermi arc in the central disjoint electron-like contour with its spin texture originating from the adjacent WSM surface [in Fig. 4(b)]. The spin texture at the top WSM/SC interface (both l_z=15 and l_z=16) results in a net spin polarization, as shown in Fig. 4(b) and (c). This spin polarization suppresses the superconductivity near the WSM/SC interfaces and drives the 'switching' transitions.

Discussion.—For the realization of the switching effect, a robust coupling between the WSM and the SC at the interface is needed [59]. The coexistence of the spin polarization and the superconductivity is observed at metallic point contacts in the WSM TaAs [39]. For practical purpose, a trilayer such as TaAs/Nb/TaAs is a testable platform [38]. The strength of the external magnetic field, used in this study, is smaller than the critical field of the superconductor (≈0.4 T for Nb [60]) and realizable in experiments. The switching effect can be controlled by tuning the chemical potential in the SC and by changing the thickness of the SC slab [59].

In the existing FM/SC/FM-based switching devices, the presence of Néel domains leads to the coexistence of both standard ($R_p>R_{ap}$) and inverse ($R_p<R_{ap}$) switching effects [52]. In the proposed WSM/SC/WSM-based switching mechanism, the unanticipated coexistence of the standard and the inverse switching effects is not possible. Also, the strong spin-momentum locking and the small Coulomb interaction in WSMs ensure a sharp switching, free from the possible Coulomb-drag or magneto-Coulomb effect [61–63].

To conclude, we predict a new magnetic-switching mechanism in WSM/SC/WSM heterostructures, which employs the strong spin-momentum locking and the surface spin polarization of the WSMs. We showed that a sharp switching phenomenon arises due to the

interplay between the WSM surface magnetization, superconductivity, and the external magnetic field. The switching effect is testable using a WSM, with either broken time-reversal symmetry or broken inversion symmetry, and has the potential for novel spin-valve applications.

Acknowledgements.—N.M. thanks A. Matos-Abiague for discussions and helpful suggestions. This work was supported by the U.S. Department of Energy (DOE), Office of Science, Basic Energy Sciences (BES), Materials Sciences and Engineering Division.

[1] B. Q. Lv, S. Muff, T. Qian, Z. D. Song, S. M. Nie, N. Xu, P. Richard, C. E. Matt, N. C. Plumb, L. X. Zhao, G. F. Chen, Z. Fang, X. Dai, J. H. Dil, J. Mesot, M. Shi, H. M. Weng, and H. Ding, "Observation of Fermi-arc spin texture in TaAs," Phys. Rev. Lett. **115**, 217601 (2015).
[2] Y. Sun, S.-C. Wu, and B. Yan, "Topological surface states and Fermi arcs of the noncentrosymmetric Weyl semimetals TaAs, TaP, NbAs, and NbP," Phys. Rev. B **92**, 115428 (2015).
[3] A. C. Potter, I. Kimchi, and A. Vishwanath, "Quantum oscillations from surface Fermi arcs in Weyl and Dirac semimetals," Nat. Commun. **5**, 5161 (2014).
[4] P. J. W. Moll, N. L. Nair, T. Helm, A. C. Potter, I. Kimchi, A. Vishwanath, and J. G. Analytis, "Transport evidence for Fermi-arc-mediated chirality transfer in the Dirac semimetal Cd_3As_2," Nature **535**, 266 (2016).
[5] P. J. W. Moll, A. C. Potter, N. L. Nair, B. J. Ramshaw, K. A. Modic, S. Riggs, B. Zeng, N. J. Ghimire, E. D. Bauer, R. Kealhofer, F. Ronning, and J. G. Analytis, "Magnetic torque anomaly in the quantum limit of Weyl semimetals," Nat. Commun. **7**, 12492 (2016).
[6] H. B. Nielsen and M. Ninomiya, "The Adler-Bell-Jackiw anomaly and Weyl fermions in a crystal," Phys. Lett. B **130**, 389 (1983).
[7] K. Fukushima, D. E. Kharzeev, and H. J. Warringa, "Chiral magnetic effect," Phys. Rev. D **78**, 074033 (2008).
[8] D. T. Son and B. Z. Spivak, "Chiral anomaly and classical negative magnetoresistance of Weyl metals," Phys. Rev. B **88**, 104412 (2013).
[9] H.-J. Kim, K.-S. Kim, J.-F. Wang, M. Sasaki, N. Satoh, A. Ohnishi, M. Kitaura, M. Yang, and L. Li, "Dirac versus Weyl fermions in Topological insulators: Adler-Bell-Jackiw anomaly in transport phenomena," Phys. Rev. Lett. **111**, 246603 (2013).
[10] A. A. Burkov, "Chiral anomaly and diffusive magnetotransport in Weyl metals," Phys. Rev. Lett. **113**, 247203 (2014).
[11] C.-Z. Li, L.-X. Wang, H. Liu, J. Wang, Z.-M. Liao, and D.-P. Yu, "Giant negative magnetoresistance induced by the chiral anomaly in individual Cd_3As_2 nanowires," Nat. Commun. **6**, 10137 (2015).
[12] X. Huang, L. Zhao, Y. Long, P. Wang, D. Chen, Z. Yang, H. Liang, M. Xue, H. Weng, Z. Fang, X. Dai, and G. Chen, "Observation of the chiral-anomaly-induced negative magnetoresistance in 3D Weyl semimetal TaAs," Phys. Rev. X **5**, 031023 (2015).
[13] Q. Li, D. E. Kharzeev, C. Zhang, Y. Huang, I. Pletikosic, A. V. Fedorov, R. D. Zhong, J. A. Schneeloch, G. D. Gu, and T. Valla, "Chiral magnetic effect in $ZrTe_5$," Nat. Phys. **12**, 550 (2016).
[14] Q. Li and D. E. Kharzeev, "Chiral magnetic effect in condensed matter systems," Nucl. Phys. A **956**, 107 (2016).
[15] Y. Li, L. Li, J. Wang, T. Wang, X. Xu, C. Xi, C. Cao, and J. Dai, "Resistivity plateau and negative magnetoresistance in the topological semimetal $TaSb_2$," Phys. Rev. B **94**, 121115 (2016).
[16] Z. Wang, Y. Zheng, Z. Shen, Y. Lu, H. Fang, F. Sheng, Y. Zhou, X. Yang, Y. Li, C. Feng, and Z.-A. Xu, "Helicity-protected ultrahigh mobility Weyl fermions in NbP," Phys. Rev. B **93**, 121112 (2016).
[17] J. Klotz, S.-C. Wu, C. Shekhar, Y. Sun, M. Schmidt, M. Nicklas, M. Baenitz, M. Uhlarz, J. Wosnitza, C. Felser, and B. Yan, "Quantum oscillations and the Fermi surface topology of the Weyl semimetal NbP," Phys. Rev. B **93**, 121105 (2016).
[18] D. E. Kharzeev, "The chiral magnetic effect and anomaly-induced transport," Prog. Part. Nucl. Phys. **75**, 133 (2014).
[19] P. Baireuther, J. A. Hutasoit, J. Tworzydło, and C. W. J. Beenakker, "Scattering theory of the chiral magnetic effect in a Weyl semimetal: interplay of bulk Weyl cones and surface Fermi arcs," New J. Phys. **18**, 045009 (2016).
[20] K. Taguchi, T. Imaeda, M. Sato, and Y. Tanaka, "Photovoltaic chiral magnetic effect in Weyl semimetals," Phys. Rev. B **93**, 201202 (2016).
[21] S. Nandy, G. Sharma, A. Taraphder, and S. Tewari, "Chiral Anomaly as the Origin of the Planar Hall Effect in Weyl Semimetals," Phys. Rev. Lett. **119**, 176804 (2017).
[22] Y.-T. Lin, L.-J. Zhai, and C.-Y. Mou, "Scaling of the chiral magnetic effect in quantum diffusive Weyl semimetals," Phys. Rev. B **97**, 245121 (2018).
[23] D. E. Kharzeev, Y. Kikuchi, and R. Meyer, "Chiral magnetic effect without chirality source in asymmetric Weyl semimetals," Eur. Phys. J. B **91**, 83 (2018).
[24] P. Li, W. Wu, Y. Wen, C. Zhang, J. Zhang, S. Zhang, Z. Yu, S. A. Yang, A. Manchon, and X.-x. Zhang, "Spin-momentum locking and spin-orbit torques in magnetic nano-heterojunctions composed of Weyl semimetal WTe_2," Nat. Commun. **9**, 3990 (2018).
[25] S.-Y. Xu, I. Belopolski, D. S. Sanchez, M. Neupane, G. Chang, K. Yaji, Z. Yuan, C. Zhang, K. Kuroda, G. Bian, C. Guo, H. Lu, T.-R. Chang, N. Alidoust, H. Zheng, C.-C. Lee, S.-M. Huang, C.-H. Hsu, H.-T. Jeng, A. Bansil, T. Neupert, F. Komori, T. Kondo, S. Shin, H. Lin, S. Jia, and M. Z. Hasan, "Spin polarization and texture of the Fermi arcs in the Weyl fermion semimetal TaAs," Phys. Rev. Lett. **116**, 096801 (2016).
[26] B. Feng, Y.-H. Chan, Y. Feng, R.-Y. Liu, M.-Y. Chou, K. Kuroda, K. Yaji, A. Harasawa, P. Moras, A. Barinov, W. Malaeb, C. Bareille, T. Kondo, S. Shin, F. Komori, T.-C. Chiang, Y. Shi, and I. Matsuda, "Spin texture in type-II Weyl semimetal WTe_2," Phys. Rev. B **94**, 195134 (2016).
[27] G. Y. Cho, J. H. Bardarson, Y.-M. Lu, and J. E. Moore, "Superconductivity of doped Weyl semimetals: Finite-

momentum pairing and electronic analog of the ^{3}He-A phase," Phys. Rev. B **86**, 214514 (2012).
[28] G. Bednik, A. A. Zyuzin, and A. A. Burkov, "Superconductivity in Weyl metals," Phys. Rev. B **92**, 035153 (2015).
[29] P. Hosur, X. Dai, Z. Fang, and X.-L. Qi, "Time-reversal-invariant topological superconductivity in doped Weyl semimetals," Phys. Rev. B **90**, 045130 (2014).
[30] T. Meng and L. Balents, "Weyl superconductors," Phys. Rev. B **86**, 054504 (2012).
[31] A. Chen and M. Franz, "Superconducting proximity effect and Majorana flat bands at the surface of a Weyl semimetal," Phys. Rev. B **93**, 201105 (2016).
[32] P. Baireuther, J. Tworzydło, M. Breitkreiz, İ Adagideli, and C. W. J. Beenakker, "Weyl-Majorana solenoid," New J. Phys. **19**, 025006 (2017).
[33] Y. Qi, P. G. Naumov, M. N. Ali, C. R. Rajamathi, W. Schnelle, O. Barkalov, M. Hanfland, S.-C. Wu, C. Shekhar, Y. Sun, V. Süß, M. Schmidt, U. Schwarz, E. Pippel, P. Werner, R. Hillebrand, T. Förster, E. Kampert, S. Parkin, R. J. Cava, C. Felser, B. Yan, and S. A. Medvedev, "Superconductivity in Weyl semimetal candidate $MoTe_2$," Nat. Commun. **7**, 11038 (2016).
[34] P. Lu, J.-S. Kim, J. Yang, H. Gao, J. Wu, D. Shao, B. Li, D. Zhou, J. Sun, D. Akinwande, D. Xing, and J.-F. Lin, "Origin of superconductivity in the Weyl semimetal WTe_2 under pressure," Phys. Rev. B **94**, 224512 (2016).
[35] F. C. Chen, X. Luo, R. C. Xiao, W. J. Lu, B. Zhang, H. X. Yang, J. Q. Li, Q. L. Pei, D. F. Shao, R. R. Zhang, L. S. Ling, C. Y. Xi, W. H. Song, and Y. P. Sun, "Superconductivity enhancement in the S-doped Weyl semimetal candidate $MoTe_2$," Appl. Phys. Lett. **108**, 162601 (2016).
[36] H. Wang, H. Wang, Y. Chen, J. Luo, Z. Yuan, J. Liu, Y. Wang, S. Jia, X.-J. Liu, J. Wei, and J. Wang, "Discovery of tip induced unconventional superconductivity on Weyl semimetal," Sci. Bull. **62**, 425 (2017).
[37] Z. Guguchia, F. von Rohr, Z. Shermadini, A. T. Lee, S. Banerjee, A. R. Wieteska, C. A. Marianetti, B. A. Frandsen, H. Luetkens, Z. Gong, S. C. Cheung, C. Baines, A. Shengelaya, G. Taniashvili, A. N. Pasupathy, E. Morenzoni, S. J. L. Billinge, A. Amato, R. J. Cava, R. Khasanov, and Y. J. Uemura, "Signatures of the topological s+- superconducting order parameter in the type-II Weyl semimetal Td-$MoTe_2$," Nat. Commun. **8**, 1082 (2017).
[38] M. D. Bachmann, N. Nair, F. Flicker, R. Ilan, T. Meng, N. J. Ghimire, E. D. Bauer, F. Ronning, J. G. Analytis, and P. J. W. Moll, "Inducing superconductivity in Weyl semimetal microstructures by selective ion sputtering," Sci. Adv. **3**, 5 (2017).
[39] L. Aggarwal, S. Gayen, S. Das, R. Kumar, V. Süß, C. Felser, C. Shekhar, and G. Sheet, "Mesoscopic superconductivity and high spin polarization coexisting at metallic point contacts on Weyl semimetal TaAs," Nat. Commun. **8**, 13974 (2017).
[40] U. Khanna, A. Kundu, S. Pradhan, and S. Rao, "Proximity-induced superconductivity in Weyl semimetals," Phys. Rev. B **90**, 195430 (2014).
[41] V. S. Speriosu, J. P. Nozieres, B. A. Gurney, B. Dieny, T. C. Huang, and H. Lefakis, "Role of interfacial mixing in giant magnetoresistance," Phys. Rev. B **47**, 11579 (1993).
[42] J. S. Moodera, J. Nowak, and R. J. M. van de Veerdonk, "Interface Magnetism and Spin Wave Scattering in Ferromagnet-Insulator-Ferromagnet Tunnel Junctions," Phys. Rev. Lett. **80**, 2941 (1998).
[43] A. I. Buzdin, A. V. Vedyayev, and N. V. Ryzhanova, "Spin-orientation-dependent superconductivity in F/S/F structures," Europhys. Lett. **48**, 686 (1999).
[44] L. R. Tagirov, "Low-Field Superconducting Spin Switch Based on a Superconductor /Ferromagnet Multilayer," Phys. Rev. Lett. **83**, 2058 (1999).
[45] S. Takahashi, H. Imamura, and S. Maekawa, "Spin imbalance and magnetoresistance in ferromagnet/superconductor/ferromagnet double tunnel junctions," Phys. Rev. Lett. **82**, 3911 (1999).
[46] I. Baladié, A. Buzdin, N. Ryzhanova, and A. Vedyayev, "Interplay of superconductivity and magnetism in superconductor/ferromagnet structures," Phys. Rev. B **63**, 054518 (2001).
[47] J. Y. Gu, C.-Y. You, J. S. Jiang, J. Pearson, Ya. B. Bazaliy, and S. D. Bader, "Magnetization-Orientation Dependence of the Superconducting Transition Temperature in the Ferromagnet-Superconductor-Ferromagnet System: CuNi/Nb/CuNi," Phys. Rev. Lett. **89**, 267001 (2002).
[48] A. Potenza and C. H. Marrows, "Superconductor-ferromagnet CuNi/Nb/CuNi trilayers as superconducting spin-valve core structures," Phys. Rev. B **71**, 180503 (2005).
[49] V. Peña, Z. Sefrioui, D. Arias, C. Leon, J. Santamaria, J. L. Martinez, S. G. E. te Velthuis, and A. Hoffmann, "Giant Magnetoresistance in Ferromagnet/Superconductor Superlattices," Phys. Rev. Lett. **94**, 057002 (2005).
[50] A. Yu. Rusanov, S. Habraken, and J. Aarts, "Inverse spin switch effects in ferromagnet-superconductor-ferromagnet trilayers with strong ferromagnets," Phys. Rev. B **73**, 060505 (2006).
[51] I. K. Yanson, Yu. G. Naidyuk, V. V. Fisun, A. Konovalenko, O. P. Balkashin, L. Yu. Triputen, and V. Korenivski, "Surface spin-valve effect," Nano Lett. **7**, 927 (2007).
[52] J. Zhu, X. Cheng, C. Boone, and I. N. Krivorotov, "Origin of the inverse spin switch effect in superconducting spin valves," Phys. Rev. Lett. **103**, 027004 (2009).
[53] J. Salafranca and S. Okamoto, "Unconventional proximity effect and inverse spin-switch behavior in a model Manganite-Cuprate-Manganite trilayer system," Phys. Rev. Lett. **105**, 256804 (2010).
[54] G. De Simoni, E. Strambini, J. S. Moodera, F. S. Bergeret, and F. Giazotto, "Toward the absolute spin-valve effect in superconducting tunnel junctions," Nano Lett. **18**, 6369 (2018).
[55] K. Halterman, O. T. Valls, and M. Alidoust, "Spin-Controlled Superconductivity and Tunable Triplet Correlations in Graphene Nanostructures," Phys. Rev. Lett. **111**, 046602 (2013).
[56] L. Majidi and R. Asgari, "Valley- and spin-switch effects in molybdenum disulfide superconducting spin valve," Phys. Rev. B **90**, 165440 (2014).
[57] M. Alidoust and K. Halterman, "Half-metallic superconducting triplet spin multivalves," Phys. Rev. B **97**, 064517 (2018).
[58] T. M. McCormick, I. Kimchi, and N. Trivedi, "Minimal models for topological Weyl semimetals," Phys. Rev. B **95**, 075133 (2017).
[59] For more information, see the Supplemental Material.

[60] W. H. Butler, "Upper Critical Field of Nb: Calculated Temperature Dependence and Anisotropy," Phys. Rev. Lett. **44**, 1516 (1980).
[61] G. Vignale, "Observing the spin coulomb drag in spin-valve devices," Phys. Rev. B **71**, 125103 (2005).
[62] S. J. van der Molen, N. Tombros, and B. J. van Wees, "Magneto-Coulomb effect in spin-valve devices," Phys. Rev. B **73**, 220406 (2006).
[63] D. D. Hiep, M. Tanaka, and P. N. Hai, "Inverse spin-valve effect in nanoscale si-based spin-valve devices," J. Appl. Phys. **122**, 223904 (2017).

Supplemental Materials

1. Hamiltonian for the middle superconductor:

In Eq. (3) of the main text, we used a mean-field Hamiltonian for the middle SC layer. Below we describe the standard mean-field decomposition of an interacting Hamiltonian to obtain a non-interacting one which is quadratic in fermionic operators and used in Eq. (3). The full Hamiltonian describing the attractive pairing interaction inside the SC slab is written as

$$\mathcal{H}_s = \sum_{\mathbf{k},\sigma} \xi_k d^\dagger_{\mathbf{k},\sigma} d_{\mathbf{k},\sigma} + \frac{1}{N}\sum_{kk'} U_{kk'} d^\dagger_{\mathbf{k},\uparrow} d^\dagger_{-\mathbf{k},\downarrow} d_{-\mathbf{k}',\downarrow} d_{\mathbf{k}',\uparrow} \tag{E1}$$

where the first term represents the kinetic energy of electrons, $\xi_k{=}-2t_s(\cos k_x + \cos k_y + \cos k_z) - \mu_s$, N is the total number of momenta in the Brillouin zone and $U_{kk'}$ is the strength of the boson-induced effective interaction between electrons at momenta $\mathbf{k}$ and $\mathbf{k}'$. The quartic term in the above Hamiltonian is decoupled into quadratic terms using the usual mean field theory: $\langle d^\dagger_{\mathbf{k},\uparrow} d^\dagger_{-\mathbf{k},\downarrow} d_{-\mathbf{k}',\downarrow} d_{\mathbf{k}',\uparrow}\rangle \approx \langle d^\dagger_{\mathbf{k},\uparrow} d^\dagger_{-\mathbf{k},\downarrow}\rangle d_{-\mathbf{k}',\downarrow} d_{\mathbf{k}',\uparrow} + d^\dagger_{\mathbf{k},\uparrow} d^\dagger_{-\mathbf{k},\downarrow}\langle d_{-\mathbf{k}',\downarrow} d_{\mathbf{k}',\uparrow}\rangle - \langle d^\dagger_{\mathbf{k},\uparrow} d^\dagger_{-\mathbf{k},\downarrow}\rangle\langle d_{-\mathbf{k}',\downarrow} d_{\mathbf{k}',\uparrow}\rangle$.
With the mean-field order parameter

$$\Delta_k = \frac{1}{N}\sum_{k'} U_{kk'}\langle d_{\mathbf{k}',\uparrow} d_{-\mathbf{k}',\downarrow}\rangle, \tag{E2}$$

the Hamiltonian $\mathcal{H}_s$ becomes

$$\mathcal{H}_s = \sum_{\mathbf{k},\sigma}\xi_k d^\dagger_{\mathbf{k},\sigma} d_{\mathbf{k},\sigma} + \sum_{\mathbf{k}}(\Delta_k d^\dagger_{\mathbf{k},\uparrow} d^\dagger_{-\mathbf{k},\downarrow} + H.c.) - \sum_{\mathbf{k}}\Delta_k\langle d^\dagger_{\mathbf{k},\uparrow} d^\dagger_{-\mathbf{k},\downarrow}\rangle. \tag{E3}$$

For pairing at zero center-of-mass momentum ($|\mathbf{k}{-}\mathbf{k}'|{=}0$) and for isotropic s-wave superconductivity ($\Delta_k{=}\Delta_s$ and $U_{kk'}{=}U_0$), the above equation becomes the following

$$\mathcal{H}_s = \sum_{\mathbf{k},\sigma}\xi_k d^\dagger_{\mathbf{k},\sigma} d_{\mathbf{k},\sigma} + \sum_{\mathbf{k}}(\Delta_s d^\dagger_{\mathbf{k},\uparrow} d^\dagger_{-\mathbf{k},\downarrow} + H.c.) + \frac{N\Delta_s^2}{|U_0|} \tag{E4}$$

which is the same Hamiltonian expressed in Eq. (3) of the main text. The above Hamiltonian is converted into a slab Hamiltonian as described below.

2. Hamiltonian for the trilayer heterostructure:

To derive the Hamiltonian of the WSM/SC/WSM heterostructure, we first obtain the Hamiltonian for the WSM and the SC slabs separately and then couple the three Hamiltonian matrices via a tunneling Hamiltonian matrix. In the slab geometry, we consider open boundary conditions along the z direction and periodic boundary conditions along the x and y directions. Below, we present the derivation for the Hamiltonian of the WSM slab and similar procedure is used to obtain the Hamiltonian for the SC slab.

The choice of the boundary conditions allows us to perform a partial Fourier transformation of the fermionic operators as $\Psi_{\mathbf{k}}{=}(1/N_w)e^{ik_z l_z}\Psi_{k_x,k_y,l_z}$, where N_w is the total number of layers inside the WSM slab along the z direction and l_z is the real-space layer index. The Hamiltonian $\mathcal{H}^{sc}_w$ (Eq. (2) in the main text) is converted to a slab Hamiltonian by writing it as

$$\mathcal{H}^{sc}_{w,slab} = \sum_{\mathbf{k}}\Psi^\dagger_{\mathbf{k}}\mathcal{H}^{sc}_w\Psi_{\mathbf{k}} = \frac{1}{N_w^2}\sum_{\mathbf{k}}\sum_{l_z,l'_z} e^{-ik_z l_z}\Psi^\dagger_{k_x,k_y,l_z}\mathcal{H}^{sc}_w e^{ik_z l'_z}\Psi_{k_x,k_y,l'_z}. \tag{E5}$$

With the exponential forms of the sine and cosine functions and the identities $\sum_{k_z} e^{ik_z(l_z-l'_z-1)}{=}N_w\delta_{z,l'_z+1}$, $\sum_{k_z} e^{ik_z(l_z-l'_z+1)}{=}N_w\delta_{z,l'_z-1}$, Eq. (E5) becomes

$$\mathcal{H}^{sc}_{w,slab} = \frac{1}{N_w}\sum_{\mathbf{k}^\parallel}\Big(\sum_{l_z=1}^{N_w}\Psi^\dagger_{\mathbf{k}^\parallel,l_z}\mathcal{H}_0(\mathbf{k}^\parallel)\Psi_{\mathbf{k}^\parallel,l_z} + \sum_{l_z=1}^{N_w-1}\big[\Psi^\dagger_{\mathbf{k}^\parallel,l_z}\mathcal{H}_1\Psi_{\mathbf{k}^\parallel,l_z+1} + H.c.\big]\Big), \tag{E6}$$

where $\mathbf{k}^\parallel{\equiv}(k_x,k_y)$, $\mathcal{H}_0(\mathbf{k}^\parallel)$ is the Hamiltonian for a single layer in the k_x-k_y plane within the WSM slab and is given by

$$\mathcal{H}_0 = \begin{pmatrix} \mathcal{H}^\parallel_w & i\sigma_y\Delta_w \\ -i\sigma_y\Delta^*_w & -\mathcal{H}^{\parallel,*}_w \end{pmatrix}, \tag{E7}$$

with $\mathcal{H}^\parallel_w = -[m(2-\cos k_y) + 2t_x(\cos k_x - \cos k_0)]\sigma_x - (2t\sin k_y)\sigma_y$. The interlayer coupling, described by Hamiltonian $\mathcal{H}_1$, is given by

$$\mathcal{H}_1 = \begin{pmatrix} \mathcal{H}^\perp_w & 0 \\ 0 & -\mathcal{H}^{\perp,*}_w \end{pmatrix}, \tag{E8}$$

where $\mathcal{H}^\perp_w = m/2\sigma_x + it\sigma_z$. Following the same prescription as above, the Hamiltonian $\mathcal{H}_s(\mathbf{k})$ (Eq. (3) in main text) is transformed into a slab Hamiltonian.

In the main manuscript, we consider a geometry in which the top and the bottom WSMs have opposite alignments of the surface Fermi arcs. This is achieved by reversing the order of the layers along the z direction in the slab Hamiltonian matrices for the top and the bottom WSM slabs. This type of alignment can also be realized in the experiment by performing a 180° rotation of the top WSM slab sample in the x-y plane after locating the direction of the surface spin polarization.

3. Calculation of the order parameters:

The superconducting order parameters, the pairing

amplitudes at each layer l_z of the heterostructure, is obtained by the self-consistent calculation, described below. The pairing amplitude $\Delta_{s,l_z}=\langle d_{\mathbf{k}^{\parallel},l_z,\uparrow}d_{-\mathbf{k}^{\parallel},l_z,\downarrow}\rangle$, at layer l_z inside the SC, is obtained by minimizing the free energy of the heterostructure Hamiltonian. To obtain the fee energy, we first write down the partition function as below

$$\mathcal{Z} = Tr[e^{-\beta\mathcal{H}_{het}}], \tag{E9}$$

where $\mathcal{H}_{het}$ is the full Hamiltonian of the WSM/SC/WSM heterostructure, $\beta{=}1/k_BT$, k_B is the Boltzmann constant and T is the temperature. The grand canonical free energy $\mathcal{F}=-1/\beta\ln\mathcal{Z}$ is given by

$$\mathcal{F} = -\frac{1}{N_k\beta}\sum_{\mathbf{k}^{\parallel},\lambda,l_z}\ln(1+e^{-\beta E_{\mathbf{k}^{\parallel}\lambda}}) - \sum_{l_z}\frac{N_k\Delta^2_{s,l_z}}{U_0}, \tag{E10}$$

where N_k is the total number of momenta in the two-dimensional Brillouin zone in each layer and $E_{\mathbf{k}^{\parallel}\lambda}$ is the λ^{th} eigen value of the heterostructure at momentum $\mathbf{k}^{\parallel}$. The set of self-consistency equations for Δ_{s,l_z} is given by setting $\partial\mathcal{F}/\partial\Delta_{s,l_z}{=}0$

$$\Delta_{s,l_z} = \frac{U_0}{2N_k}\sum_{\mathbf{k}^{\parallel},\lambda}\frac{\partial E_{\mathbf{k}^{\parallel}\lambda}}{\partial\Delta_{s,l_z}}\tanh\Big(\frac{\beta E_{\mathbf{k}^{\parallel}\lambda}}{2}\Big). \tag{E11}$$

We start with a finite initial value of Δ_{s,l_z} and update them iteratively until self-consistency is achieved at each layer l_z.

The pairing amplitude $\Delta_{w,l_z}=\langle c_{\mathbf{k}^{\parallel},l_z,\uparrow}c_{-\mathbf{k}^{\parallel},l_z,\downarrow}\rangle$ at layer l_z inside the WSM is calculated using the four-component spinor wave functions, extracted from the converged wave function of $\mathcal{H}_{het}$, and using the usual Bogoliubov-Valatin transformation $c_{\mathbf{k}^{\parallel},l_z,\sigma}{=}\sum_\lambda u^{\lambda}_{\mathbf{k}^{\parallel},l_z,\sigma}\gamma_\lambda{+}v^{\lambda*}_{\mathbf{k}^{\parallel},l_z,\sigma}\gamma^{\dagger}_{\lambda}$, where $u^{\lambda}_{\mathbf{k}^{\parallel},l_z,\sigma}\gamma_\lambda$ ($v^{\lambda}_{\mathbf{k}^{\parallel},l_z,\sigma}\gamma_\lambda$) is the quasiparticle (quasihole) amplitude and γ_λ ($\gamma^{\dagger}_{\lambda}$) is the fermionic annihilation (creation) operator. The pairing amplitude Δ_{w,l_z} is then obtained using

$$\Delta_{w,l_z} = \sum_{\mathbf{k}^{\parallel},\lambda}\Big[u^{\lambda}_{\mathbf{k}^{\parallel},l_z,\uparrow}v^{\lambda*}_{\mathbf{k}^{\parallel},l_z,\downarrow}(1-f(E_{\mathbf{k}^{\parallel}\lambda})) + u^{\lambda}_{\mathbf{k}^{\parallel},l_z,\downarrow}v^{\lambda*}_{\mathbf{k}^{\parallel},l_z,\uparrow}f(E_{\mathbf{k}^{\parallel}\lambda})\Big], \tag{E12}$$

where $f(E_{\mathbf{k}^{\parallel}\lambda})$ is the Fermi function at temperature T and energy $E_{\mathbf{k}^{\parallel}\lambda}$.

The magnetization components at each layer l_z and momentum $\mathbf{k}^{\parallel}$ is obtained by taking the expectation values of the Pauli matrices in the particle-hole space, τ_α (where $\alpha{=}x,y,z$), on the calculated wave function $\Psi_{\mathbf{k}^{\parallel},l_z}$ as follows

$$m_{\mathbf{k}^{\parallel},l_z,\alpha} = \frac{\hbar}{2}\Big\langle\Psi_{\mathbf{k}^{\parallel},l_z}\Big|\tau_\alpha\Big|\Psi_{\mathbf{k}^{\parallel},l_z}\Big\rangle, \tag{E13}$$

where $\Psi_{\mathbf{k}^{\parallel},l_z}{=}\big(c_{\mathbf{k}^{\parallel},l_z,\uparrow},c_{\mathbf{k}^{\parallel},l_z,\downarrow}c^{\dagger}_{-\mathbf{k}^{\parallel},l_z,\downarrow},c^{\dagger}_{-\mathbf{k}^{\parallel},l_z,\uparrow}\big)$ for the WSM slab, and similar for the SC slab with $c_{\mathbf{k}^{\parallel},l_z,\sigma}$ (here $\sigma{=}\uparrow,\downarrow$) operators replaced by $d_{\mathbf{k}^{\parallel},l_z,\sigma}$ operators.

4. Layer-resolved profile of the pairing amplitude at different field angles:

In Fig. S1, we show the variation of the layer-resolved pairing amplitude Δ_{l_z} at different field angles θ of the applied magnetic field. This result supports the main finding discussed in the main text *i.e.* there are two distinct ranges of θ *viz.* (a) the suppressed and (b) the enhanced superconducting states. The profile of Δ_{l_z} remains almost the same within the range $100°{\leq}\theta{\leq}260°$. For the considered SC slab of thickness $N_s{=}15$, the reappearance of superconductivity takes place near the WSM/SC interfaces. The superconductivity in the central layers of the SC can also by recovered fully by reducing the thickness N_s. In the main manuscript, we considered $N_s{=}15$ to fully resolve the spatial region in which the interplay between superconductivity and magnetism takes place. For an experimental demonstration of the discussed switching effect, a very thin SC slab would be beneficial.

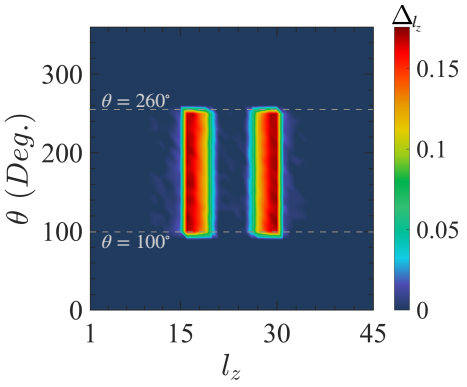

FIG. S1. Layer-resolved pairing amplitude Δ_{l_z} at different angle θ of the applied magnetic field $B{=}0.1t$. Other parameters are the same as in Fig. (2) of the main manuscript.

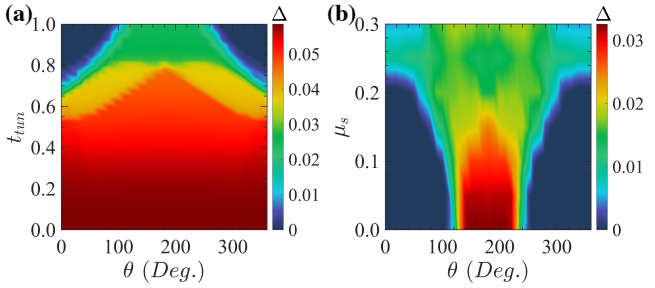

FIG. S2. Variation of the mean superconducting pairing amplitude Δ of the trilayer heterostructure with magnetic-field angle θ and (a) the WSM-SC tunneling amplitude t_{tun} and (b) the chemical potential μ_s in the SC slab. Other parameters, unless otherwise stated, are the same as in Fig. (2) of the main manuscript.

5. External control on the switching effect:

The magnetic-field induced switching effect, which is discussed in the main manuscript, can be controlled by a number of ways. In Fig. S2, we show the modulation of the mean superconducting pairing amplitude by the

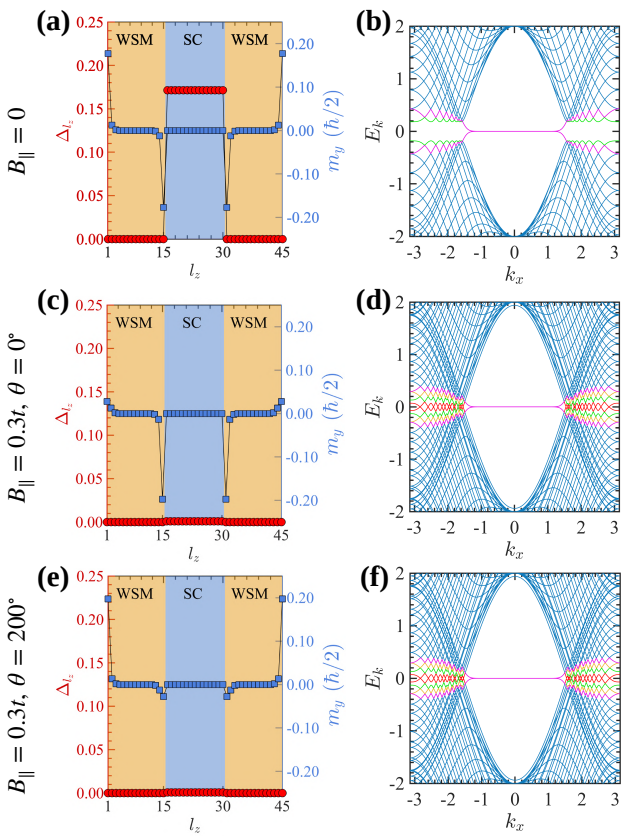

FIG. S3. (a),(c),(e) Variation of the superconducting pairing amplitude Δ_{l_z} (left vertical axis) and y component of magnetization m_y (right vertical axis) with the layer index l_z at (a) magnetic field $B_\parallel$=0, (c) $B_\parallel$=0.3t, θ=0° and (e) $B_\parallel$=0.3t, θ=200°. (b), (d) and (f) show the corresponding energy spectrum of the WSM/SC/WSM heterostructure at k_y=0. The energy levels in red, green, yellow and magenta originate primarily from the surfaces of the WSMs. Parameters are the same as in Fig. 2 of the main manuscript, except t_{tun}=0.

WSM-SC tunneling amplitude t_{tun} and by the chemical potential μ_s in the SC. Fig. S2(a) indicates that a strong coupling between the SC and the WSM slabs is required to realize the proximity effect of the surface spin texture of the WSM on the superconductivity. Fig. S2(b) indicates that the switching effect is tunable by μ_s which can be modulated externally by a gate voltage.

6. Absence of the switching effect at zero WSM/SC coupling:

To understand the role of the WSM/SC interface on the observed switching effect, here we consider the case in which the WSM and the SC slabs are not connected *i.e.* t_{tun}=0. The layer-resolved pairing amplitude Δ_{lz}, and the dominant magnetization component m_y are shown in Fig. S3(a), (c) and (e), at different field scenarios and the corresponding spectrum in Fig. S3(b), (d) and (f). The magnetization inside the WSM behaves in a similar way as in the case $t_{tun}\neq$0, described in the main manuscript *i.e.* the surface magnetization decreases when the magnetic field is applied opposite to the spin polarization direction. With $t_{tun}\neq$0, both the WSM surface magnetization and the magnetic field jointly suppress the superconductivity. In the case t_{tun}=0, a higher magnetic field is required to fully suppress the superconductivity. However, this field is equal to or larger than the critical field $B_\parallel^c\approx 0.3t$ for superconductivity in the SC slab and, therefore, a reappearance of superconductivity is not possible. Furthermore, the spectra in Fig. S3(b), (d) and (f) do not reveal the reappearance of the spectral gap outside the flat-band region (*i.e.* $|k_x|>k_0$), as found in the case with $t_{tun}\neq$0. The results highlight the importance of a strongly-coupled WSM/SC interface behind the discussed switching effect.